Electronic Supplementary Information (ESI) for

Two-Dimensional Quasi-Nanosheets Enabled by Coordination-Driving Deposition and Sequential Etching

Peiying Liu,[1] Boxu Gao, [2] Cancan Wang, [1] Shaoxue Pan, [1] Zhimin Zhai, [1] Tianqi Wu, [1] Yicheng Liu, [1] Jiajia Zhang, *[1] Hongbin Lu *[1]

Email: hongbinlu@fudan.edu.cn; zhangjiajia@fdan.edu.cn

This material includes

Experimental

Computational details

Experimental

Synthesis of porous N-MO quasi-nanosheets. In a typical synthesis of $N-TiO_2$, 60 mg $TiOSO_4$, 360 μl HCl (12 M) and 1.8 g DCDA were all resolved in distilled water and stirred vigorously at 60 °C for at least 3 hours to obtain homogeneous mixture, and then was calcinated immediately at 300 °C for 20min and then maintained at 450 °C for 3h in air tube furnace. Similarly, several kinds of holey MO superstructures, such as Fe_2O_3 (60mg Ferrous Sulfate and 1.8g DCDA), NiO (60mg Nickel Acetate and 1.8g DCDA), Co_3O_4 (180mg Cobalt Acetate and 1.8g DCDA), as well as $NiCo_2O_4$ (20mg Nickel Acetate, 40mg Cobalt Acetate and 1.8g DCDA) and $CoFe_2O_4$ (60mg Nickel Acetate and 1.8g DCDA) were all prepared under similar calcination process. The control sample $N-TiO_2$ NB and $N-Co_3O_4$ NB were prepared by calcining powder mixture of DCDA and $TiOSO_4$ or cobalt ccetate with certain mass ratio.

Synthesis of porous N-FeP@C quasi-nanosheets. 10 mg as-obtained $N-Fe_2O_3$ was poured into dopamine hydrochloride solution (3 mg/ml) (PBS buffer, PH=8.5) and stirred for 1h to wrap polydopamine, and then the product was phosphatized and carbonized at 400 °C for 2 h under Ar atmosphere with 500 mg NaH_2PO_2 placed together as a phosphorus source. The control sample p-FeP@C was synthesized through phosphorization of pure Fe_2O_3 holey nanosheets (after maintaining $N-Fe_2O_3$ at 450 °C for another 5h) and Fe_2O_3 bulk without any templates.

Material characterization. X-ray diffraction (XRD) patterns were performed using a PANalytial X' Pert PRO diffractometer with Cu Kα radiation (40 kV, 40 mA). Field-emission scanning electron microscope (FESEM) images were measured on Zeiss Gemini SEM500. Transmission electron microscopy (TEM) measurements were taken on Tecnai G2 20 TWIN with a voltage of 200 kV. The

morphology, element distribution and the lattice fringe of the samples were characterized by field-emission transmission electron microscope (FETEM) 2100F. X-ray photoelectron spectroscopy (XPS) was conducted on an AXIS UltrDLD spectrometer (Shimadzu-Kratos) with Al Kα radiation as the excitation source. Thermogravimetric analysis (TGA) was measured on Pyris1 TGA (Mettler Toledo) with a heating rate of 20 $^{\circ}$C /min under air atmosphere. The Brunauer-Emmett-Teller (BET) measurement is utilized to calculate the specific surface areas of metal-based superstructures. And the pore size distributions and pore volumes are obtained from the adsorption branches of isotherms through the Barrett-Joyner-Halenda (BJH) model.

Photocatalytic measurements. 10 mg photocatalyst was added to 10 ml of 10 ppm RhB solution and stirred for 30 min in the dark to achieve adsorption/desorption equilibrium. The visible light source was provided by 300 W Xe lamp equipped with a UV light filter > 420 nm, and photocatalytic degradation were carried out at a constant temperature of 25°C. During reaction process, intermediates were intermittently taken for UV-Vis absorption analysis.

Electrochemical measurements. **Hydrogen Evolution Reaction:** All the electrochemical catalytic measurements were conducted in a standard three-electrode system (CHI660E) with carbon paper as counter electrode, graphite rod working electrode and Ag/AgCl reference electrode in 0.5 M $H2_SO_4$ solution. 1.5 mg catalyst was dispersed in 120 µl distilled water, 70 µl ethanol and 10 µl Nafion (5wt% in a mixture of ethanol and water, Sigma-Aldrich) and sonicated to get a homogeneous ink. Then, 8 µl ink was drop-cast onto the carbon paper and dried naturally. Besides, all the potentials were calibrated with an RHE followed the equation: $E_{RHE} = E_{SCE} + 0.21 V + 0.059*PH$. LSV curves were carried out from -0.6 V to -0.1 V under the sweep rate of 5 mV/s and collected after iR correction. Electrochemical impedance spectroscopic (EIS) measurements were conducted from 0.01 to 10^6 Hz at a potential of 200mV. The cyclic voltammetry curves were measured under different scan rates from 10 to 300 mV/s and corresponding Cdl were defined to be the slopes of fitted linear lines between half capacitive current density and their scan rates. **Oxygen Evolution Reaction:** All the electrochemical catalytic measurements were conducted in a standard three-electrode system (CHI660E) with carbon paper as counter electrode, graphite rod working electrode and Hg/HgO reference electrode in 1 M KOH

solution. 1 mg catalyst and 0.2 mg Super P (Conductive additive) were dispersed in 100 μl distilled water, 90 μl ethanol and 10 μl Nafion and sonicated to get a homogeneous ink. Then, 8 μl ink was drop-cast onto the carbon paper and dried naturally. Besides, all the potentials were calibrated with an RHE followed the equation: $E_{RHE} = E_{SCE} + 0.098$ V $+ 0.059*PH$. LSV curves were carried out from 0.2 V to 0.8 V under the sweep rate of 5 mV/s and collected after iR correction. Electrochemical impedance spectroscopic (EIS) measurements were conducted from 0.01 to 10^6 Hz at a potential of 550 mV. The cyclic voltammetry curves were measured under different scan rates from 2 to 10 mV/s and corresponding Cdl were defined to be the slopes of fitted lines between half capacitive current density and scan rate.

Computational details

We have employed the Vienna Ab Initio Package (VASP) [1, 2] to perform all the spin-polarized density functional theory (DFT) calculations within the generalized gradient approximation (GGA) using the PBE[3] formulation. We have chosen the projected augmented wave (PAW) potentials[4,5] to describe the ionic cores and take valence electrons into account using a plane wave basis set with a kinetic energy cutoff of 400 eV. Partial occupancies of the Kohn–Sham orbitals were allowed using the Gaussian smearing method and a width of 0.05 eV. The electronic energy was considered self-consistent when the energy change was smaller than 10^{-7} eV. A geometr y optimization was considered convergent when the energy change was smaller than 10^{-6} eV. Grimme's DFT-D3 methodology[6] was used to describe the dispersion interactions among all the atoms in the polyimide unit cell and adsorption models of interest.

The equilibrium lattice constants of orthogonal FeP bulk unit cell were optimized, when using a 7×6×11 Monkhorst-Pack k-point grid for Brillouin zone sampling, to be a=5.112 Å, b=5.722 Å, and c=3.011 Å. Bade on these, we build a FeP(011) p(1×1) surface in the x and y directions and 3 stoichiometric layers in the z direction together with 15 Å vaccum in the z direction to separate the surface from its periodic images. This surface model contains 12 Fe and 12 P atoms. During structural optimizations, a 7×6×1 Monkhorst-Pack k-point grid was used and top two stochimetric layers were allowed to fully relax while the bottom one was fixed.

The adsorption energy (Eads) of H atom was defined as Eads = $E_{H/Surf}$ - E_{Surf} - $0.5*EH_2(g)$ where $E_{H/surf}$, E_{surf} and $EH_2(g)$ are the energy of H adsorbed on the surface

model, the energy of clean surface model, and the energy of isolated H_2 molecule in a cubic periodic box with a side length of 20 Å and a 1×1×1 Monkhorst-Pack k-point grid for Brillouin zone sampling, respectively.
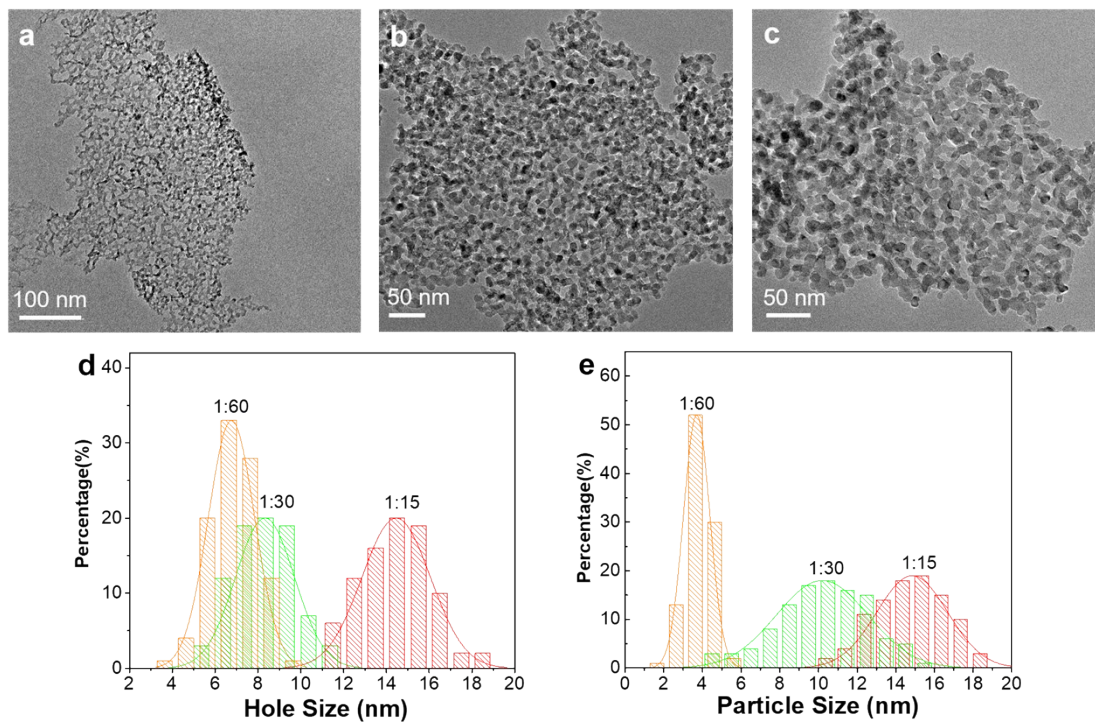

Fig. S1 TEM images of N-TiO₂ NS synthesized at different ratio (a) 1:60, (b) 1:30 and (c) 1:15. Corresponding particle sizes (d) and hole sizes (e) of N-TiO₂ NS obtained from statistics analysis of TEM.
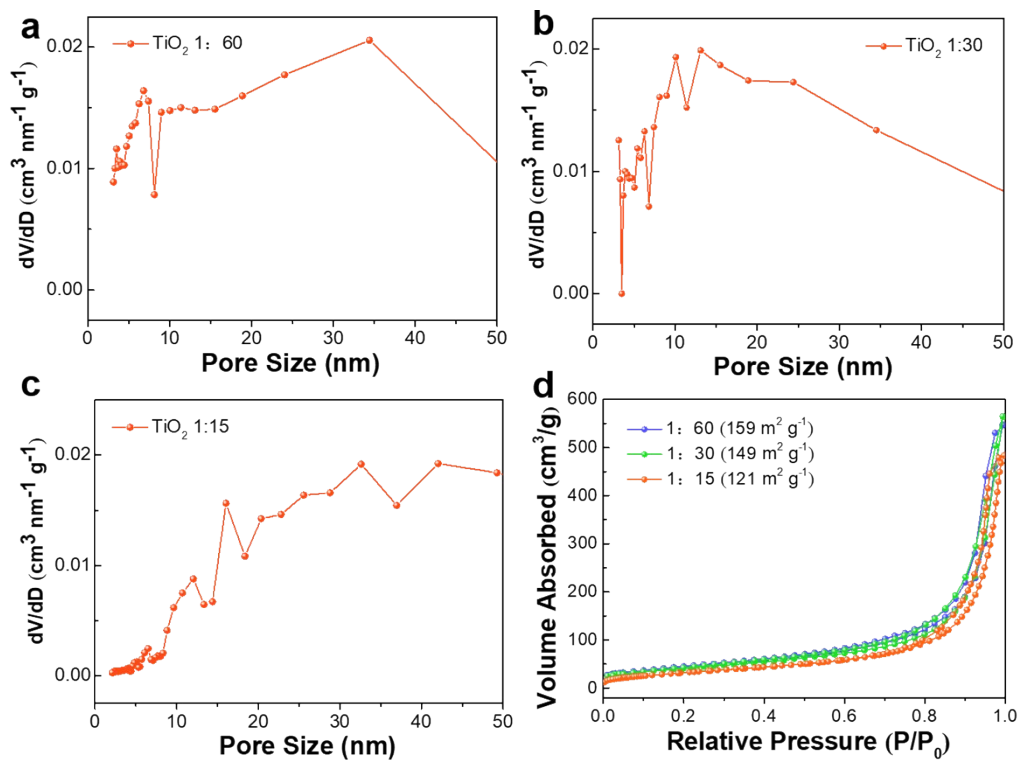
Fig. S2 BJH pore size distribution of TiO$_2$ nanosheets prepared at different mass ratio of TiOSO$_4$ and DCDA (a) TiO$_2$ 1:60, (b) TiO$_2$ 1:30 and (c) TiO$_2$ 1:15, and corresponding N$_2$ adsorption–desorption isotherms.
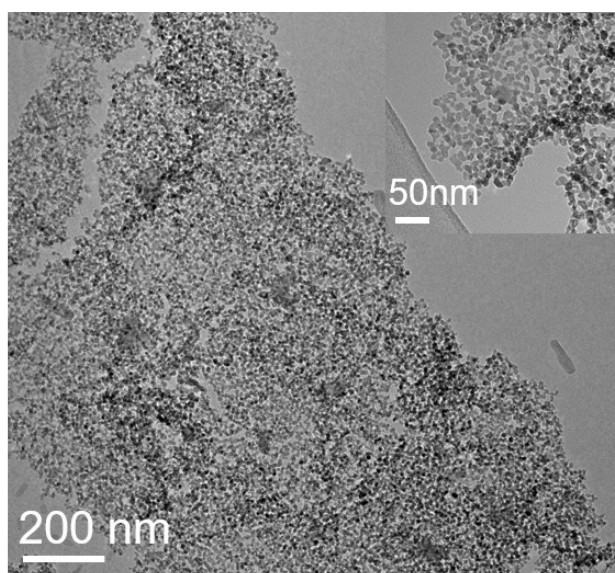
Fig. S3 TEM images of TiO$_2$ porous nanosheets after calcination at 450℃ for further 3h.
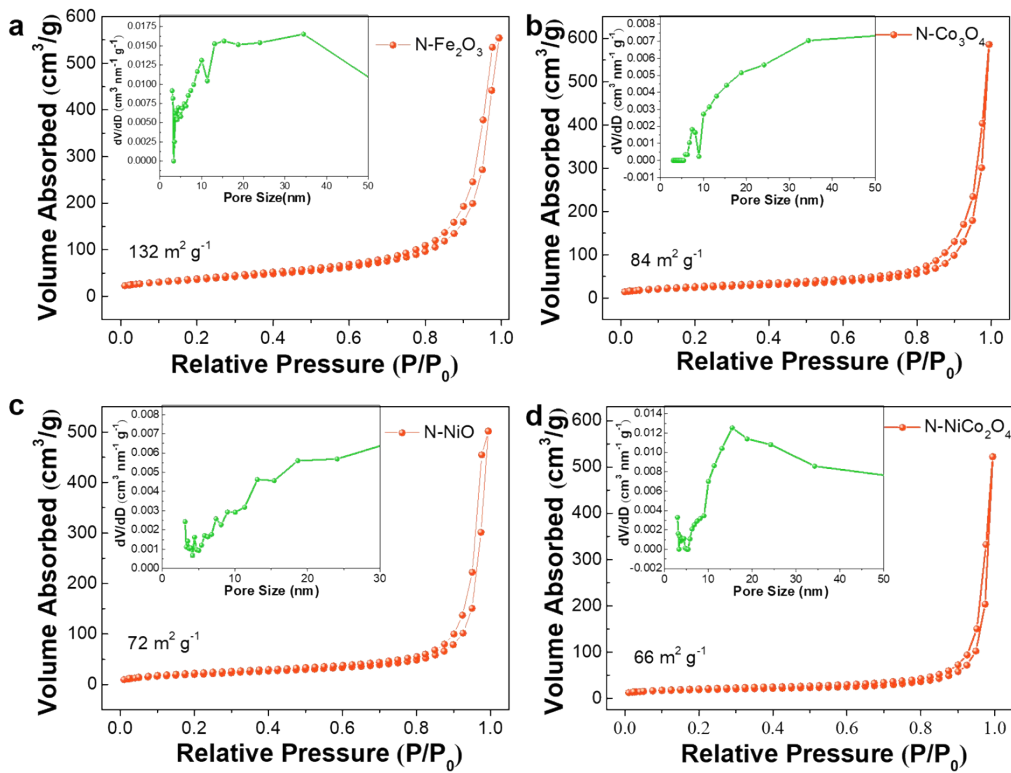
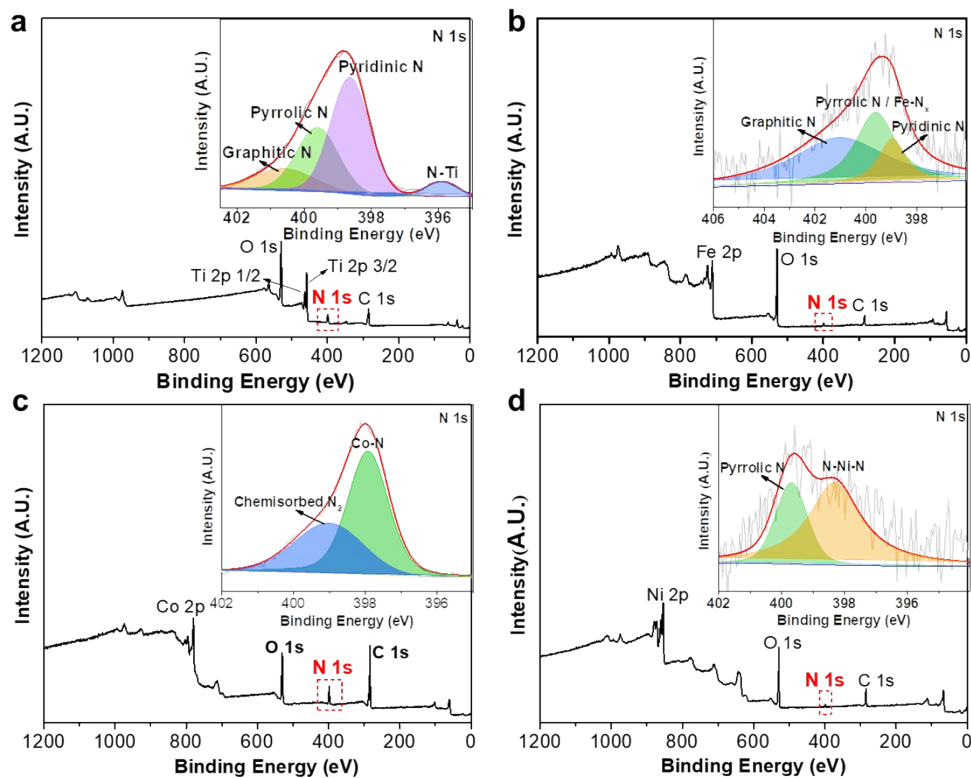**Fig. S4 N₂ desorption isotherms** N-Fe$_2$O$_3$ NS (a), N-Co$_3$O$_4$ NS (b), N-NiO NS (c) and N-NiCo$_2$O$_4$ NS (d).

Fig. S5 XPS survey spectrum and N 1s spectra of N-TiO$_2$ NS (a), N-Fe$_2$O$_3$ NS (b), N-Co$_3$O$_4$ (c) and N-NiO NS (d) holey nanosheets.
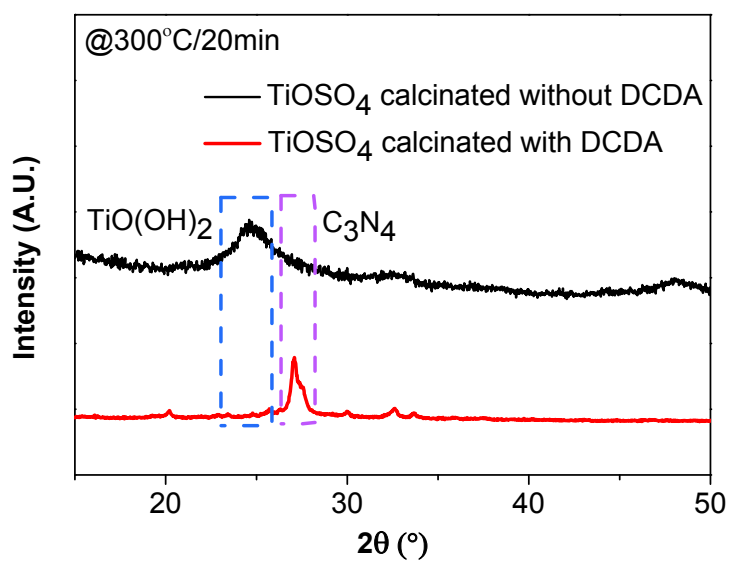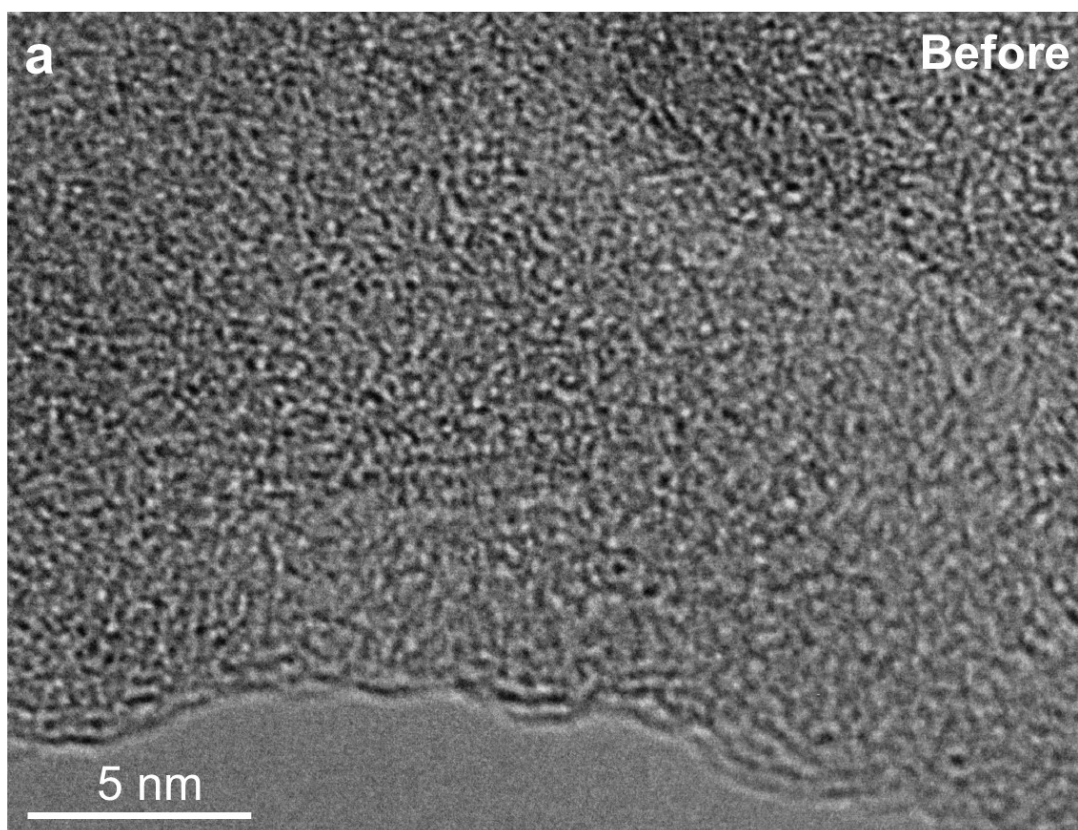
Fig. S6 XRD patterns of calcination products of $TiOSO_4$ with and without DCDA at 300°C for 20min.
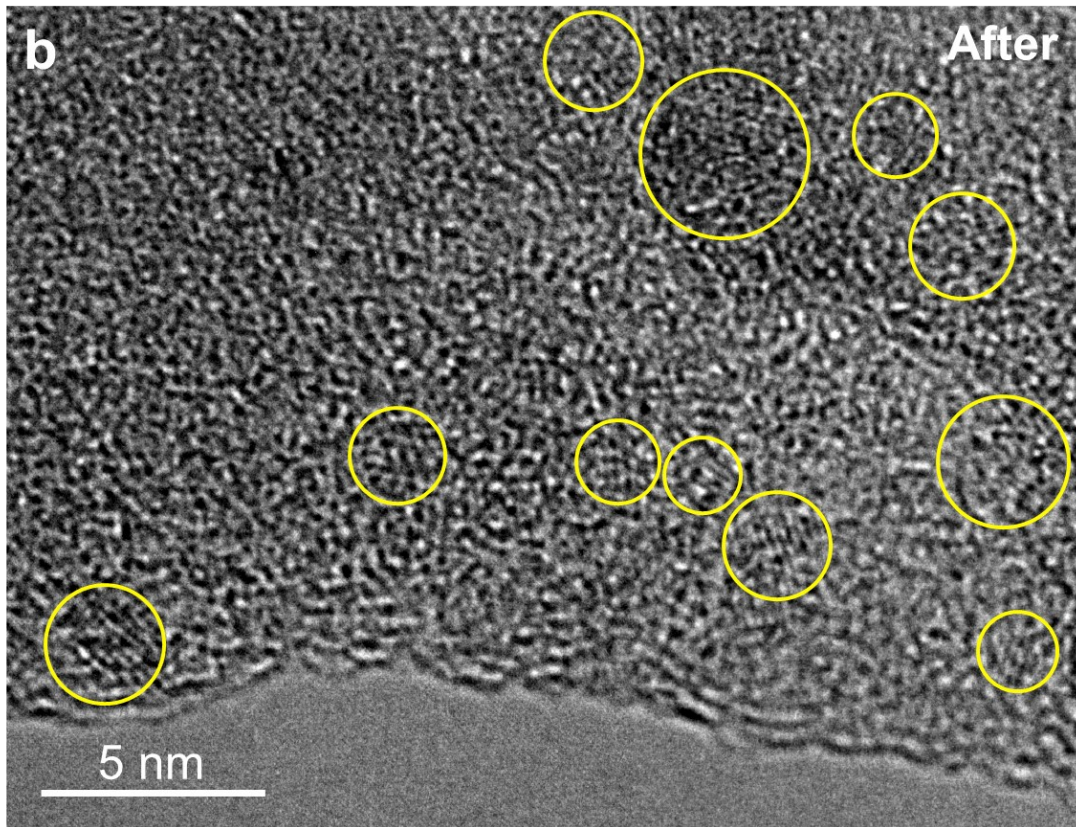
Fig. S7 In-situ high-resolution TEM images before (a) and after (b) 60-second irradiation.
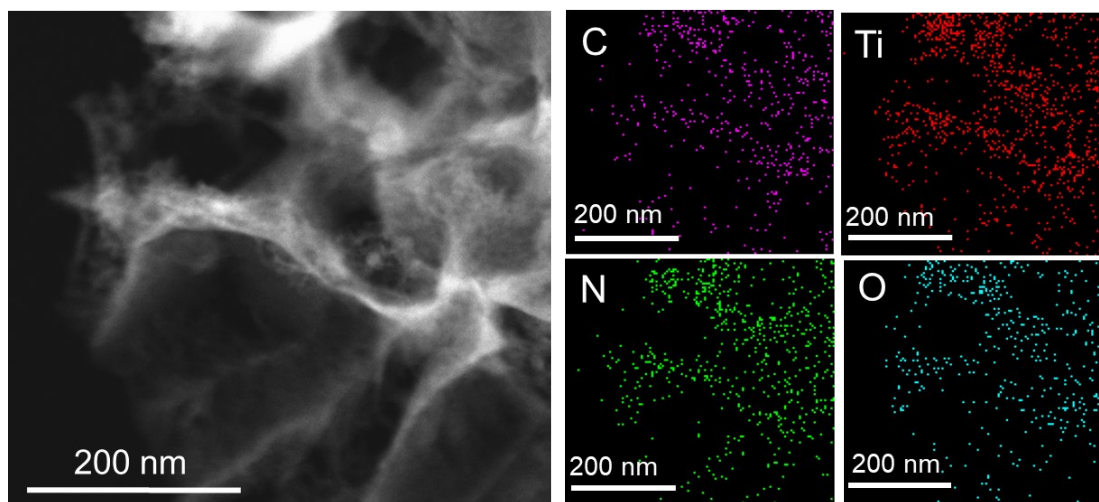

Fig. S8 STEM images and corresponding elements mapping of CN (450 ℃/60 min).
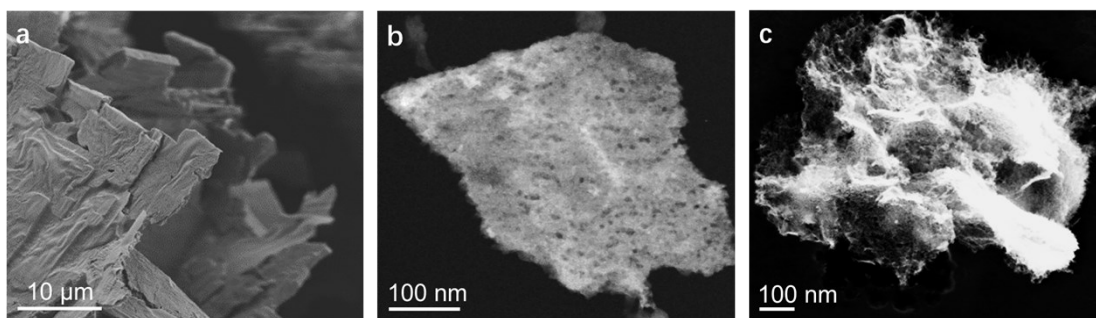
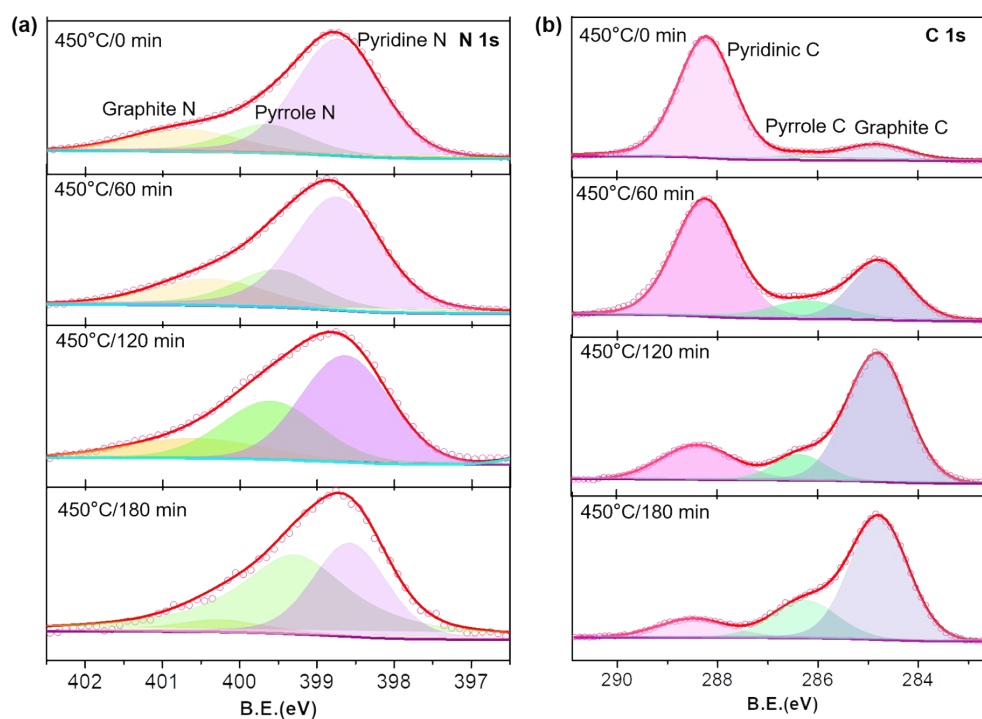**Fig. S9** SEM images of intermediates of (a) 300 °C/20 min, (b) 450 °C/60 min and (c) 450 °C/180 min.

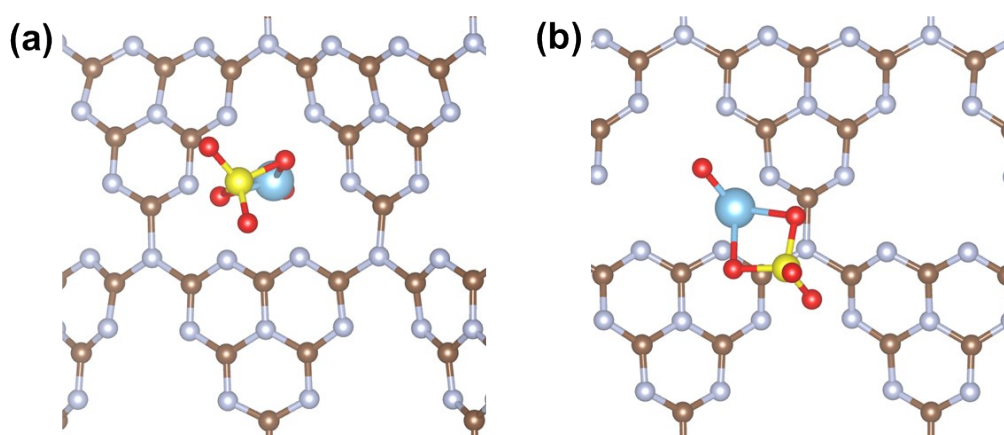**Fig. S10** XPS spectra of (a) N 1s and (b) C 1s of intermediates obtained at different stages.

Fig. S11 The adsorption configuration of TiOSO$_4$-N$_6$ (a) and TiOSO$_4$-N$_2$ (b) on CN
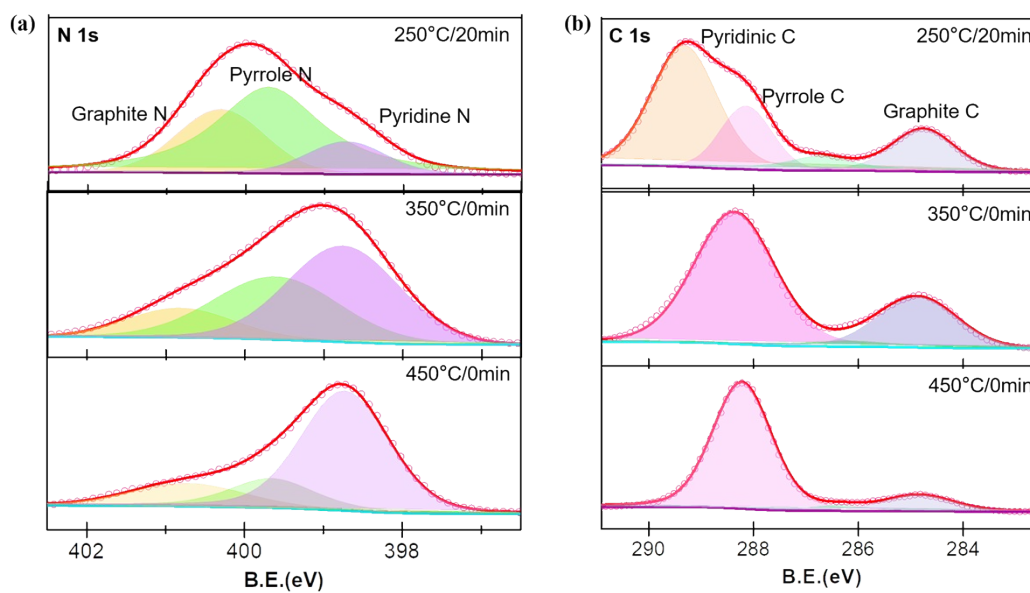
structures.

Fig. S12 XPS spectra of (a) N 1s and (b) C 1s of intermediates obtained at different stages.
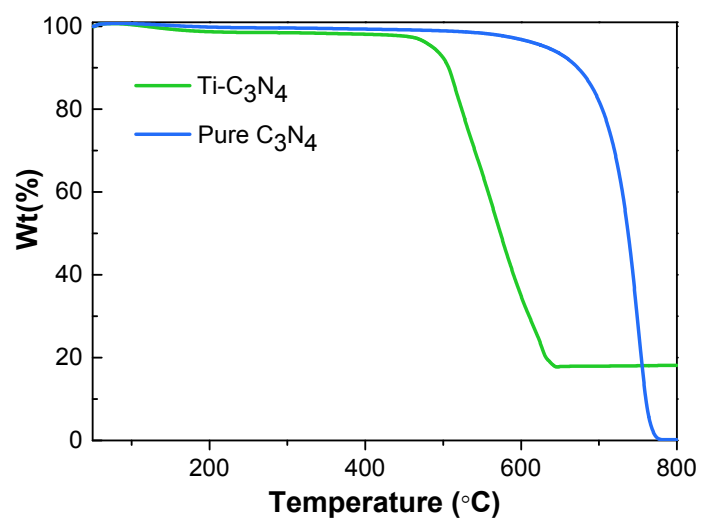

Fig. S13 TGA curves of pure CN and CN coordinated with Ti ions.
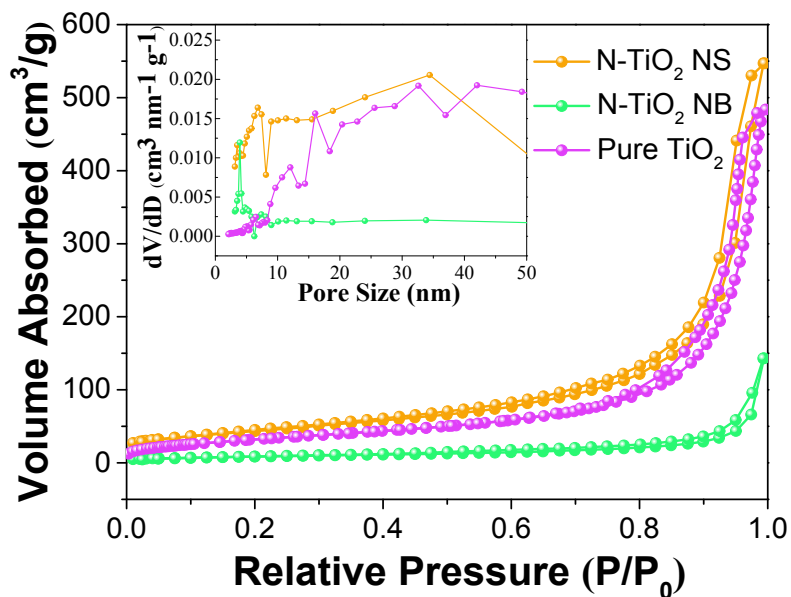
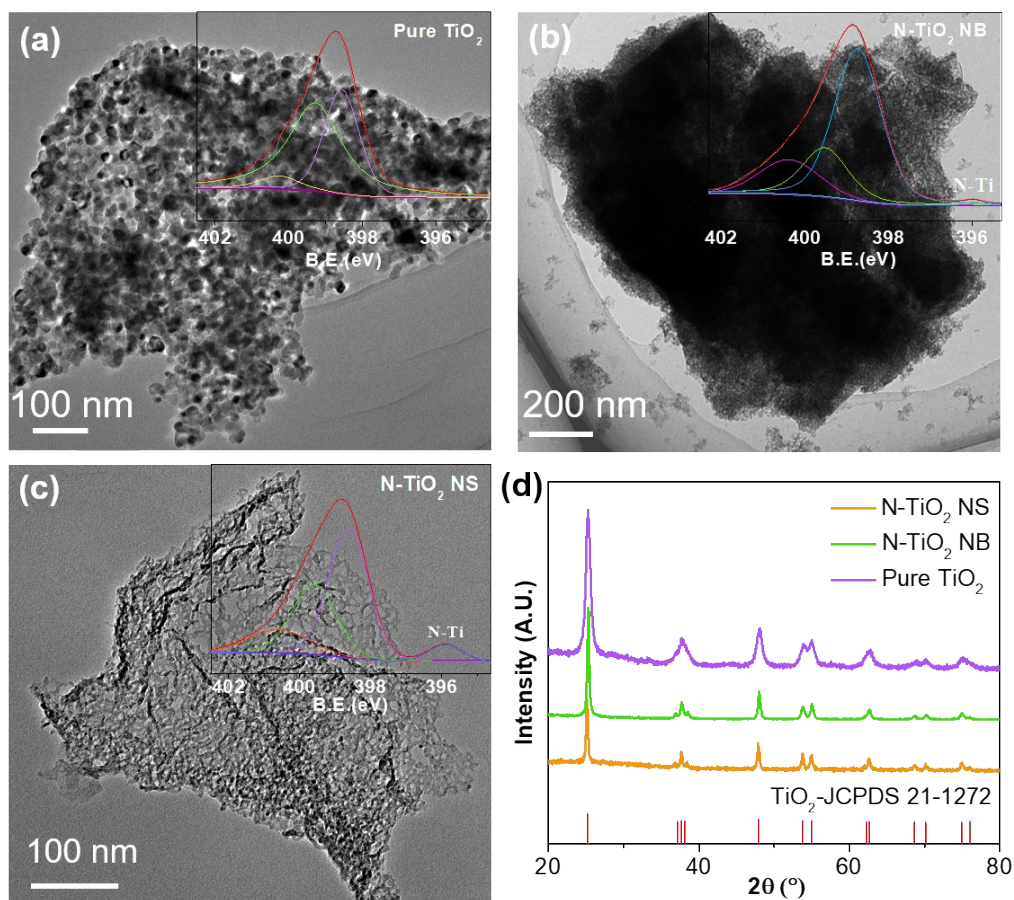**Fig. S14** N$_2$ adsorption–desorption isotherms and corresponding BJH pore size distribution of a series of TiO$_2$.

Fig. S15 TEM images of pure TiO$_2$ (a), N-TiO$_2$ NB (b) and N-TiO$_2$ NS (c), and corresponding XRD patterns (d).
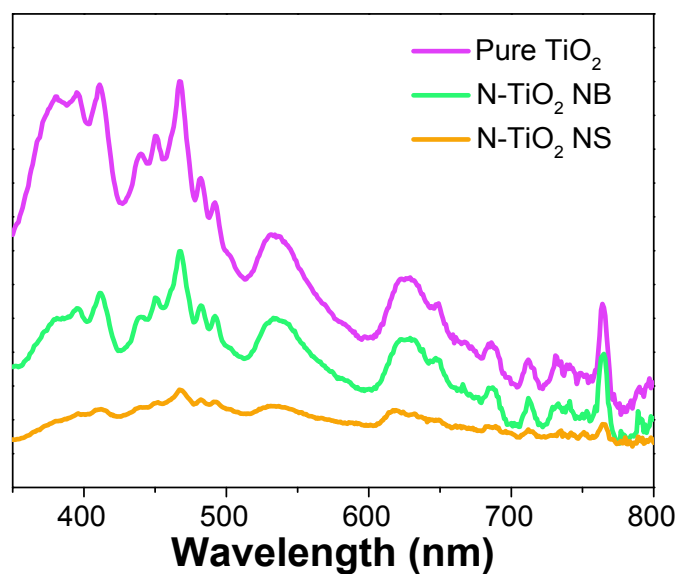
Fig. S16 PL spectra of N-TiO$_2$ NS, N-TiO$_2$ NB and Pure TiO$_2$.
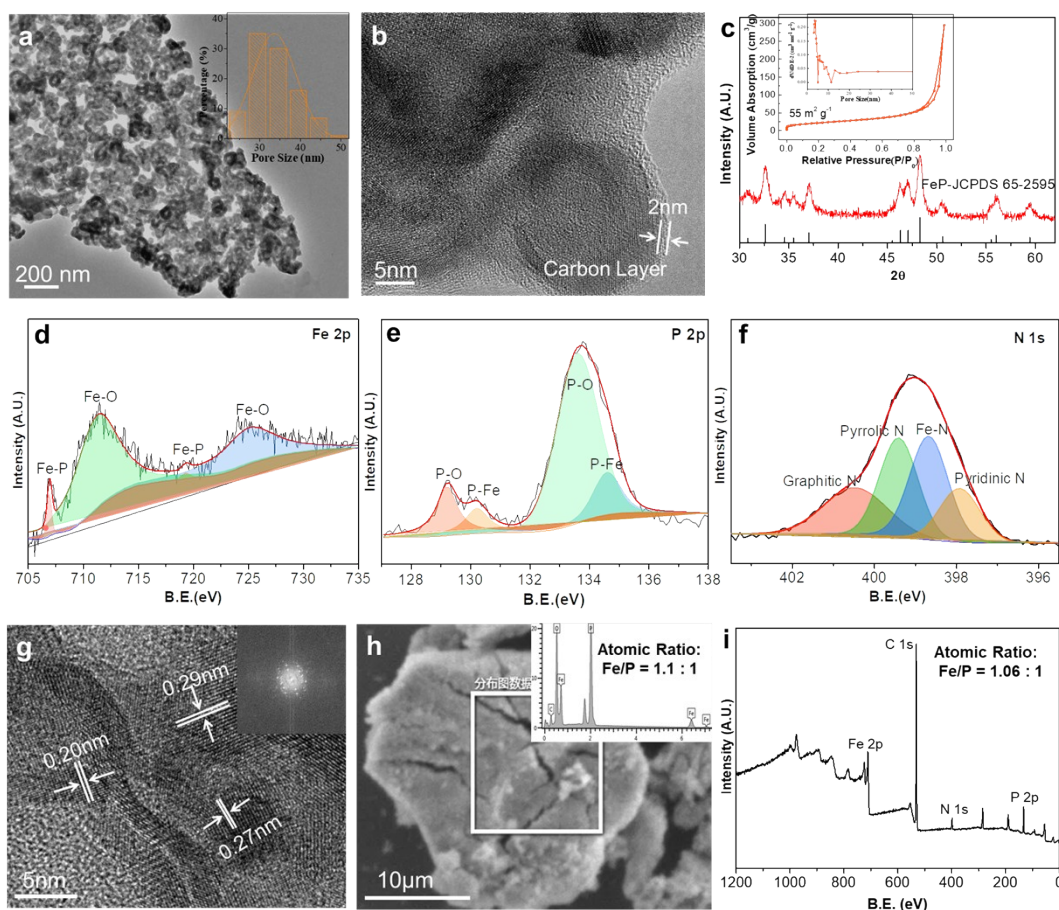

Fig. S17 Characterization of FeP@C holey nanosheets. (a) Low-magnification and (b) High-resolution TEM images of N-FeP@C NS. (c) XRD pattern of N-FeP@C NS, inset is the nitrogen adsorption-desorption isotherm. XPS spectra of Fe 2p (d), P 2p (e) and N 1s (f). SEM images (g) and EDS results of Fe and P contents of N-FeP@C NS (h), XPS survey spectrum and corresponding elements contents.

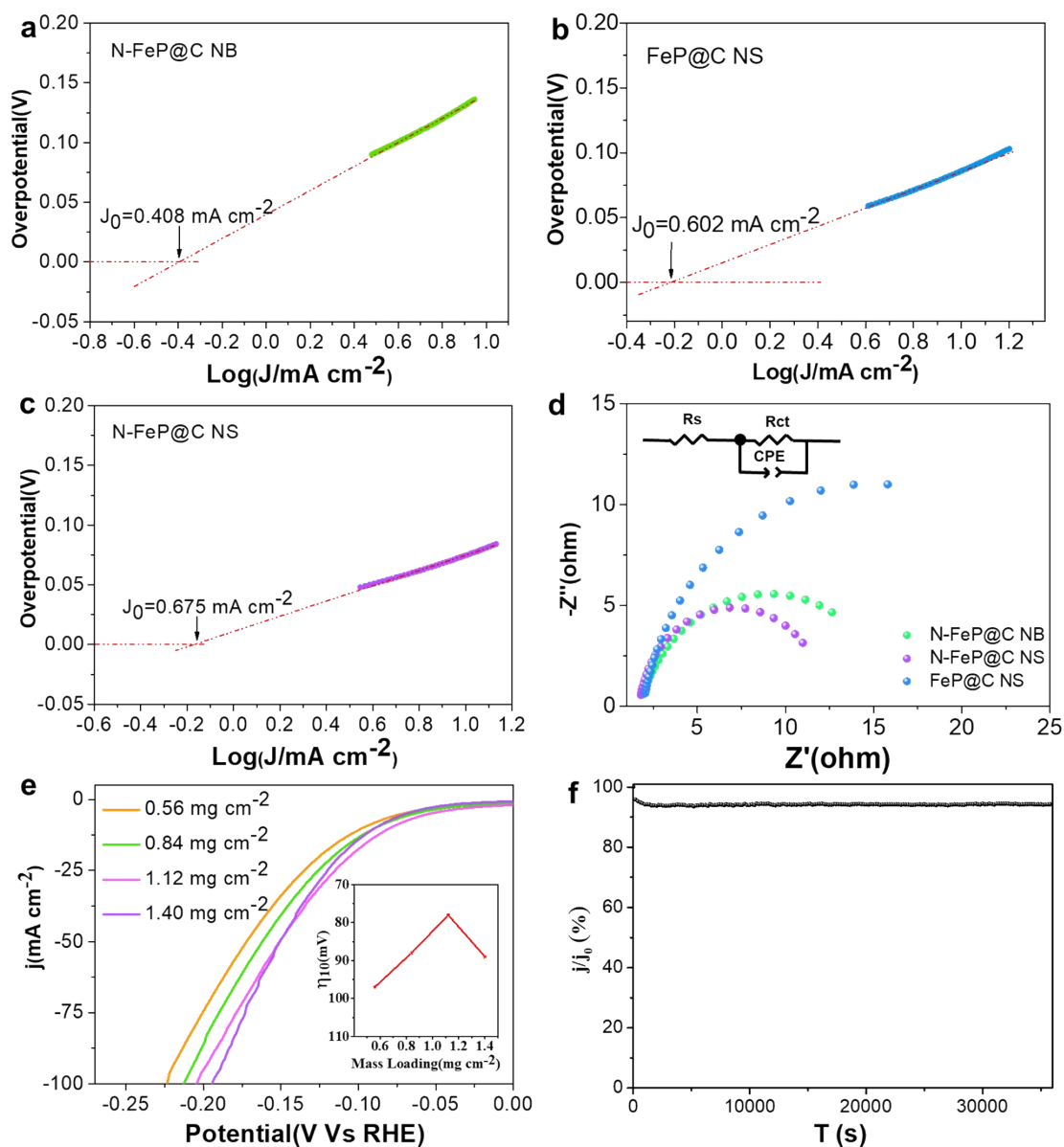**Fig. S18 Electrochemical measurements of FeP@C holey nanosheets.** Exchange current density of N-FeP@C NB (a), N-FeP@C NS (b) and FeP@C NS (c). (d) Nyquist plots and (e) Polarization curves of N-FeP@C NS with different mass loading and the inset is the relationship between mass loading and η_{10}. (f) Chronopotentiometry curves of N-FeP@C NS at a constant current density of 10 mA cm^{-2} for 10h.
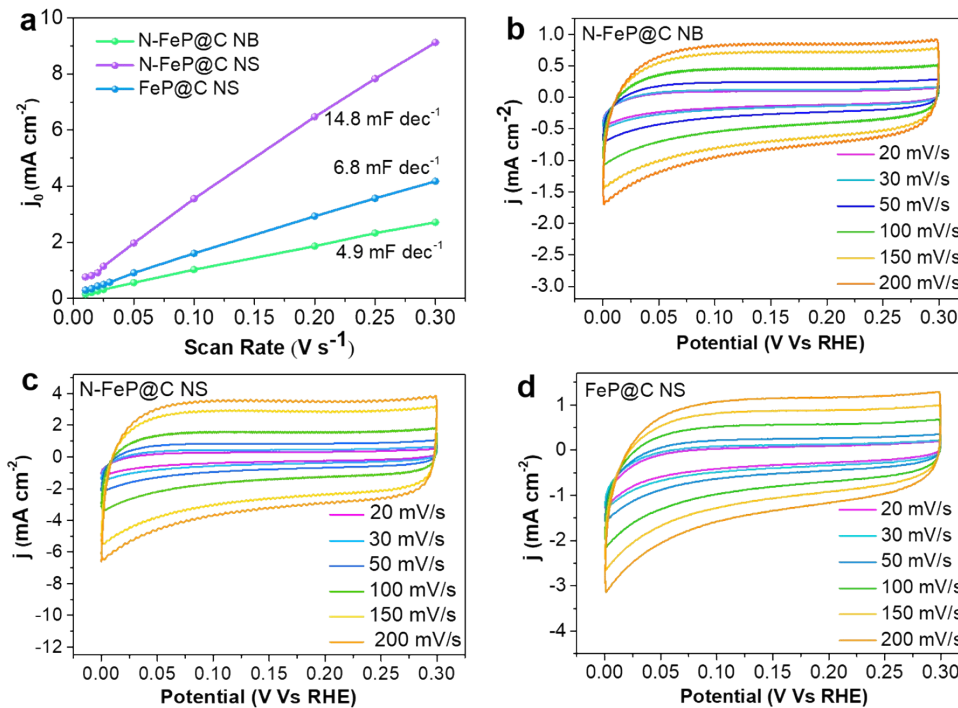
Fig. S19 C_{dl} and corresponding CV curves at different scan rates (a) comparation of a series of FeP@C catalysts , (b) N-FeP@C NB, (c) N-FeP@C NS and (d) FeP@C NS.

Table S1. Comparisons of the electrocatalytic activities of FeP@C in 0.5 M H_2SO_4 solution.

Catalyst	η@j (mV@mA cm^{-2})	Tafel slope (mV dec^{-1})	Onset η (mV)	C_{dl} (mF cm^{-2})	J_0 (mV cm^{-2})
N-FeP@C NB	139@10 178@20 257@50	91	51	6.1	0.408
N-FeP@C NS	78@10 102@20 149@50	57	25	14.8	0.675
FeP@C NS	124@10 155@20 216@50	77	46	4.9	0.602

Table S2. Comparison of the electrocatalytic activities of Transition Metal Compounds with some representative HER electrocatalysts in 0.5 M H_2SO_4 solution.

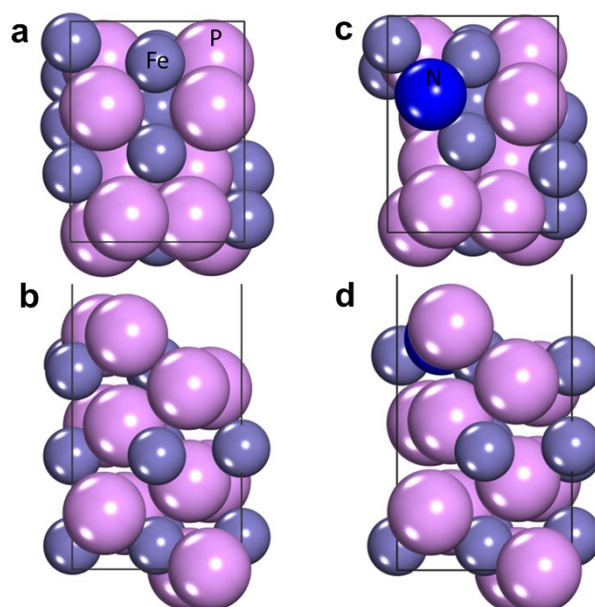| Catalyst	Tafel slope (mV dec^{-1})	η_{10} (mV)	j_0 (mA cm^{-2})	Ref.
N-FeP@C NS	60	78	0.513	This work
MoP$_2$NS/CC	63.6	58	0.83	[7]
NFP/C-3	72	54	0.723	[8]
MoP$_2$ NPs/Mo	57	143	0.06	[9]
MoCx nanooctahedrons	53	142	0.023	[10]
CoP/CC	51	67	0.288	[11]
NiCo$_2$Px/CF	60	104	N.A.	[12]
FeP NA/Ti	38	55	0.42	[13]
Fe-doped CoP/Ti	75	78	N.A.	[14]
Hollow FeP nanosheet	41.7	51.1	N.A.	[15]
CoP@BCN	46	87	4.19	[16]
FeP@C	52	71	N.A.	[17]
Pt@PCM	63.7	105	N.A.	[18]

Fig. S20 Optimized structures of FeP (011) (a top view and b side view) and N doped FeP (011) (c top view and d top view).
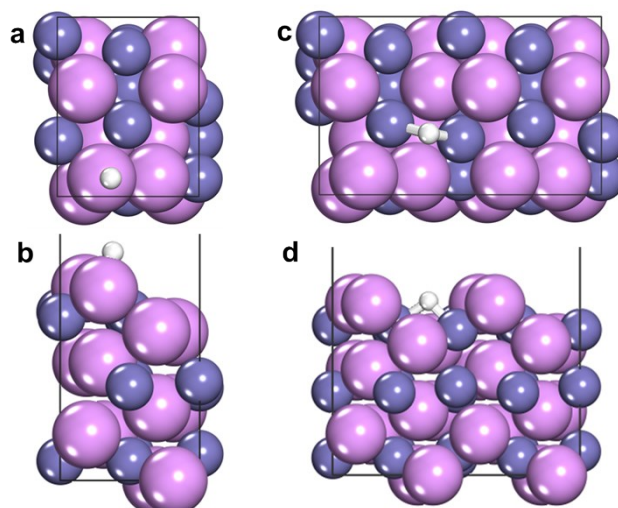
Fig. S21 Optimized configuration of H adsorption on P top sites (a top view and b side view) and Fe bridge sites of FeP (011) (c top view and d top view).
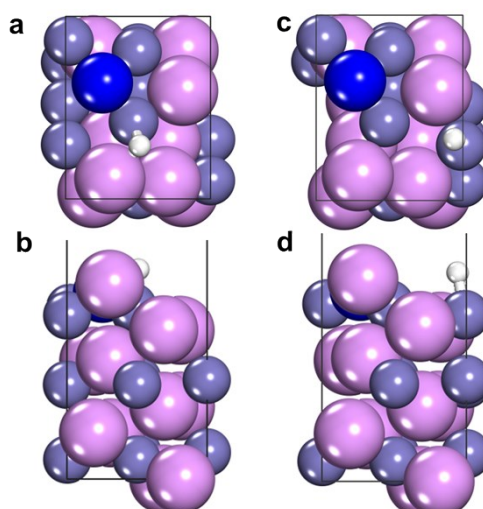

Fig. S22 Optimized configuration of H adsorption on Fe top sites (a, c top view and b, d side view) of N doped FeP (011).
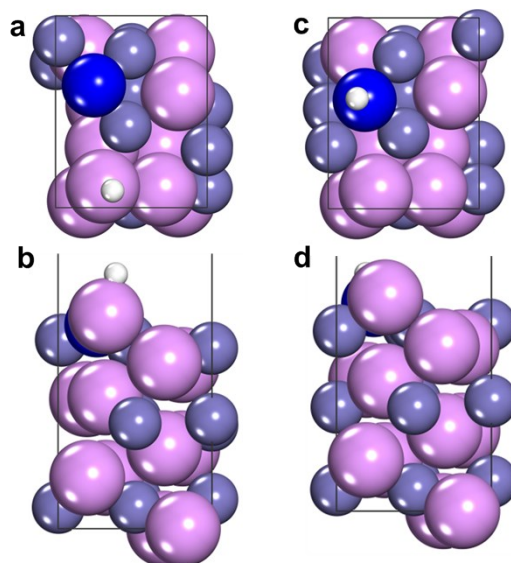
Fig. S23 Optimized configuration of H adsorption on P top sites (a top view and b side view) and N top sites of N doped FeP (011) (c top view and d top view).
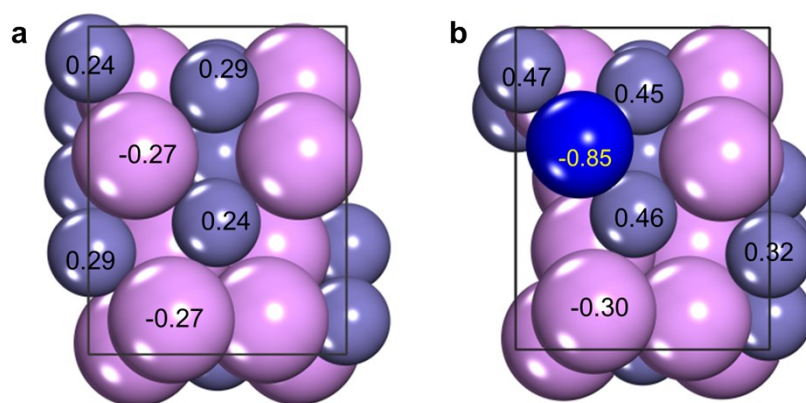

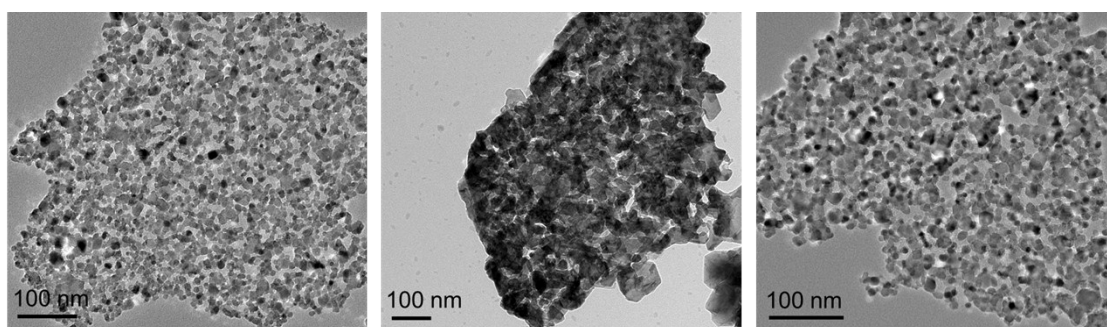**Fig. S24** Bader charge analysis and corresponding differences to pristine ionic models.

Fig. S25 TEM images of a series of Co$_3$O$_4$ catalyst. (a) N-Co$_3$O$_4$ NS, (b) N-Co$_3$O$_4$ NB, (c) Co$_3$O$_4$ NS.

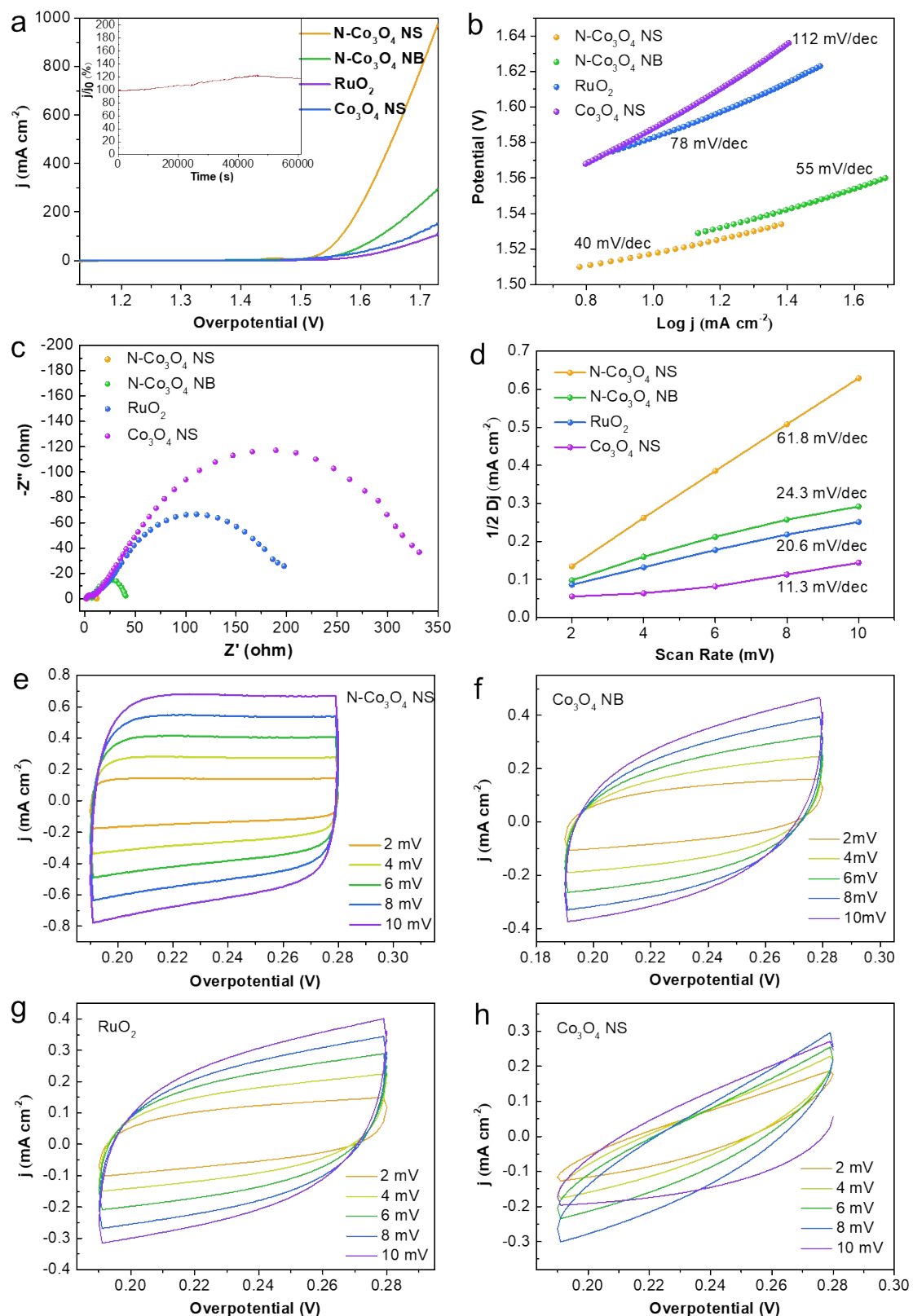**Fig. S26 Electrochemical measurements of a series of Co$_3$O$_4$ catalysts.** (a) Polarization curves of N-Co$_3$O$_4$ NS, N-Co$_3$O$_4$ NB, Co$_3$O$_4$ and RuO$_2$, and the inset is the chronoamperometry curve of N-Co$_3$O$_4$ NS at 10 mA/cm^2 for 15h. (b) Corresponding Tafel slopes, (c) Nyquist plots, (d) Cdl and (e-h) CV curves at different scan rates.

References

1 G. Kresse, J. Furthmüller, *Comput. Mater. Sci.*, 1996, **6**, 15–50.

2 G. Kresse, J. Furthmüller, *Phys. Rev. B.*, 1996, **54**, 11169–11186.

3 J. P. Perdew, K. Burke, M. Ernzerhof, *Phys. Rev. Lett.*, **1996**, 77, 3865–3868.

4 G. Kresse, D. Joubert, *Phys. Rev. B.*, 1999, **59**, 1758-1775.

5 P. B. Blöchl, *Phys. Rev. B.*, 1994, **50**, 17953–17979.

6 S. Grimme, J. Antony, S. Ehrlich, H. Krieg, *J. Chem. Phys.*, 2010, **132**, 154104.

7 H. B. Gray, *Nat. Chem.*, 2009, **1**, 7.

8 X. F. Lu, L. Yu, X. W. Lou, *Sci. Adv.*, 2019, **5**, 2.

9 Q. P. Lu, *Adv. Mater.*, 2016, **28**, 1917-1733.

10 D. Vory, R. Fuon, J. Yan, R. Kappra, I. Bozkurt, D. Kaplan, M. J. Lagos, P. E. Batson, G. Gupta, A. D. Mohite, L. Dong, D. Q. Er, V. B. Shenoy, T. Asefa, M. Chhowalla, *Nat. Mater.*, 2016, **15**, 1003-1009.

11 B. F. Cao, G. M. Veith, J. C. Neuefeind, R. R. Adzic, P. G. Khalifah, *J. Am. Chem. Soc.*, 2013, **135**, 19186-19192.

12 Zhang, R.; Wang, X.; Yu, S.; et al. Electrocatalysts: Ternary NiCo2Px Nanowires as pH-Universal Electrocatalysts for Highly Efficient Hydrogen Evolution Reaction. *Adv. Mater.*, 2017, **47**, 1605502.

13 P. Jiang, Q. Liu, Y. H. Liang, J. Q. Tian, A. M. Asiri, X. P. Sun, *Angew. Chem.-Int. Edit.*, 2014, **53**, 12855-12859.

14 C. Tang, R. Zhang, W. B. Lu, L. B. He, X. Jiang, A. M. Asiri, X. P. Sun, *Adv. Mater.*, 2017, **29**, 2, 1602441.

15 F. X. Ma, C. Y. Xu, F. C. Lyu, B. Song, S. C. Sun, Y. Y. Li, J. Lu, L. Zhen, *Adv. Sci.*, 2018, 1801490.

16 H. Tabassum, W. H. Guo, W. Meng, A. Mahmood, R. Zhao, Q. F. Wang, R. Q. Zou, *Adv. Energy Mater.*, 2017, 1601671.

17 D. Y. Chung, S. W. Jun, G. Yoon, H. Kim, J. M. Yoo, K. S. Lee, T. Kim, H. Shin, A. K. Sinha, S. G. Kwon, K. Kang, T. Hyeon, Y. E. Sung, *J. Am. Chem. Soc.*, 2017, **139**, 6669–6674.

18 H. B. Zhang, P. F. An, W. Zhou, B. Y. Guan, P. Zhang, J. C. Dong, X. W. Lou, *Sci. Adv.*, 2018, **4**.